

High temperature, low neutron cross-section high-entropy alloys in the Nb-Ti-V-Zr system

King, D. J. M.; Cheung, S. T. Y.; Humphry-Baker, S. A.; Parkin, C.; Couet, A.; Cortie, M. B.; Lumpkin, G. R.; Middleburgh, S. C.; Knowles, Alexander

DOI:

[10.1016/j.actamat.2019.01.006](https://doi.org/10.1016/j.actamat.2019.01.006)

License:

Creative Commons: Attribution-NonCommercial-NoDerivs (CC BY-NC-ND)

Document Version

Peer reviewed version

Citation for published version (Harvard):

King, DJM, Cheung, STY, Humphry-Baker, SA, Parkin, C, Couet, A, Cortie, MB, Lumpkin, GR, Middleburgh, SC & Knowles, A 2019, 'High temperature, low neutron cross-section high-entropy alloys in the Nb-Ti-V-Zr system', *Acta Materialia*, vol. 166, pp. 435-446. <https://doi.org/10.1016/j.actamat.2019.01.006>

[Link to publication on Research at Birmingham portal](#)

Publisher Rights Statement:

<https://doi.org/10.1016/j.actamat.2019.01.006>

General rights

Unless a licence is specified above, all rights (including copyright and moral rights) in this document are retained by the authors and/or the copyright holders. The express permission of the copyright holder must be obtained for any use of this material other than for purposes permitted by law.

- Users may freely distribute the URL that is used to identify this publication.
- Users may download and/or print one copy of the publication from the University of Birmingham research portal for the purpose of private study or non-commercial research.
- User may use extracts from the document in line with the concept of 'fair dealing' under the Copyright, Designs and Patents Act 1988 (?)
- Users may not further distribute the material nor use it for the purposes of commercial gain.

Where a licence is displayed above, please note the terms and conditions of the licence govern your use of this document.

When citing, please reference the published version.

Take down policy

While the University of Birmingham exercises care and attention in making items available there are rare occasions when an item has been uploaded in error or has been deemed to be commercially or otherwise sensitive.

If you believe that this is the case for this document, please contact UBIRA@lists.bham.ac.uk providing details and we will remove access to the work immediately and investigate.

High temperature, low neutron cross-section high-entropy alloys in the Nb-Ti-V-Zr system

D. J. M. King^{1,2*}, S. T. Y. Cheung¹, S. A. Humphry-Baker¹, C. Parkin³, A. Couet³, M. B. Cortie⁴, G.R. Lumpkin⁵, S. C. Middleburgh⁶, A. J. Knowles^{1,7}

¹ Centre for Nuclear Engineering, Imperial College London, South Kensington, London, SW7 2AZ, UK

² Department of Mechanical Engineering, University of New South Wales, Sydney, New South Wales, Australia, 2052

³ Department of Engineering Physics, University of Wisconsin-Madison, Madison, WI 53715, USA

⁴ School of Mathematical and Physical Sciences, University of Technology, Sydney, New South Wales, Australia, 2007

⁵ Australian Nuclear Science and Technology Organisation, Lucas Heights, New South Wales, Australia

⁶ Nuclear Futures Institute, Bangor University, Dean Street, Bangor, Wales, LL57 1UT, UK

⁷ School of Metallurgy and Materials, University of Birmingham, Birmingham, B15 2SE, UK

* Correspondence: daniel.king@imperial.ac.uk

Abstract:

High-entropy alloys (HEAs) with high melting points and low thermal neutron cross-section are promising new cladding materials for generation III+ and IV power reactors. In this study a recently developed high throughput computational screening tool Alloy Search and Predict (ASAP) has been used to identify the most likely candidate single-phase HEAs with low thermal neutron cross-section, from over a million four-element equimolar combinations. The selected NbTiVZr HEA was further studied by density functional theory (DFT) for moduli and lattice parameter, and by CALPHAD to predict phase formation with temperature. HEAs of NbTiVZr_x ($x = 0.5, 1, 2$) were produced experimentally, with Zr varied as the dominant cross-section modifier. Contrary to previous experimental work, these HEAs were demonstrated to constitute a single-phase HEA system; a result obtained using a faster cooling rate following annealing at 1200°C. However, the beta (BCC) matrix decomposed following aging at 700°C, into a combination of nano-scale beta, alpha (HCP) and C15 Laves phases.

Keywords: High-entropy alloys; Zirconium alloys; Modeling; Microstructure; Electron microscopy

1. Introduction

The concept of high-entropy alloys (HEAs)¹ removes the constraints of an alloy consisting of one predominant element, which greatly opens the composition and phase space for materials design and discovery. Since the first publications that introduced this concept [1,2] there have been many examples of HEAs, some of which offer superior properties in comparison to conventional alloys [3–6]. Conversely, there have been a large number of HEAs that exhibit complex and brittle phases/microstructures [7–10]. To avoid the latter, various methods and criteria have been developed to predict alloy stability, focusing on the formation of simple microstructures with majority solid-solution phase fractions that are associated with more ductile and workable alloys [11–14]. Configurational entropy, the namesake of HEAs, has a considerable influence on the stability of the solid solution phase at high-temperature [15]. It follows that at lower temperatures (<1000 K), at equilibrium, phase separation or intermetallic formation may occur [16]. Although this can be beneficial in terms of precipitation hardening, phase transitions during intermediate temperature operation may induce changes in dimensions and embrittlement, which are often undesirable in a

¹ Also known as multiprincipal component alloys and compositionally complex alloys.

structural material. It is therefore important to understand a HEA's thermal stability in detail, in order to identify at which point these phenomena occur.

Recently, there has been great interest in HEAs for nuclear applications due to their apparent resistance to radiation effects [17–19]. One such application is for a replacement of Zr alloys as an accident-tolerant fuel cladding in nuclear fission reactors. Zirconium alloys are currently the most widely used cladding material and favoured over steels due to their lower thermal neutron absorption cross-section, ~ 0.2 and ~ 2.0 barns, respectively [20]. However, during loss of coolant scenarios Zr alloys can undergo significant oxidation [21] and elevated temperatures will lead to the alpha to beta phase transformation inducing loss of mechanical strength resulting in ballooning of the cladding tubes and a further reduction in coolant flow [22].

By incorporating the microscopic thermal neutron absorption cross section (σ_A) into a HEA screening tool it is possible to identify new alloys that are well suited as in-core structural components for generation IV nuclear reactors, that are projected to have increased neutron flux, and operational temperature ranges of 500 – 1300 K [23,24].

The ASAP software [25] was used within the present study to find the best candidate equimolar single-phase HEA, optimised for single-phase thermodynamic stability and thermal neutron transparency. From over 1 million equimolar combinations, the Nb-Ti-V-Zr system was identified. From this system, three variant alloys NbTiVZr_{0.5}, NbTiVZr and NbTiVZr₂ (henceforth referred to as Zr_{0.5}HEA, Zr₁HEA and Zr₂HEA) were further studied. The lower temperature behaviour was predicted using CALPHAD and compared to samples homogenised and aged at 1200 and 700°C, respectively, for 100 h. Density functional theory (DFT) simulations were performed on structures modelled from the homogenised structures; lattice parameters and elastic properties were calculated and also compared to experimentally obtained values from nano-indentation.

As far as the authors are aware, experimental work on only the equimolar case has been published in previous literature [26,27], where combinations of the Cr-Nb-Ti-V-Zr system were assessed for potential low density structural materials.

2. Materials and methods

2.1 Theoretical

2.1.1 Alloy search and predict

The ability for elemental mixtures to form a single-phase solid-solution was assessed using a high-throughput method of alloy prediction implemented in the software Alloy Search and Predict (www.alloyasap.com) [28,29]. The measure of thermodynamic stability of the solid-solution phase is predicted by the Φ parameter as,

$$F = \frac{\Delta G_{ss}}{-|\Delta G_{max}|} \quad (1)$$

Where ΔG_{ss} is the Gibbs free energy of a solid-solution of the hypothetical mixture and $|\Delta G_{max}|$ is the maximum magnitude of the Gibbs free energy of a potential binary intermetallic compound that can form from the constituents, scaled to the number of elements in the solid-solution (calculated using Miedema's method for formation enthalpies of concentrated solid solutions and intermetallic compounds [30,31], respectively, and including the Gibbs entropy). A commonly used parameter for assessing the deviation in atomic radii, δ [11,32,33], between the constituents is coupled with Φ whereby for a mixture that has both $\Phi \geq 1$ and $\delta \leq 6.6$, it is predicted that a single-phase HEA could form at the melting temperature. Four-component equiatomic mixtures were searched by assessing unique combinations made from 72 elements from the periodic table.

2.1.2 Calculation of phase diagrams

The CALPHAD method was performed in Thermocalc™ using the HEA database “TCHEA2”. This database contains all binaries, as well as 135 fully and 308 tentatively assessed ternaries [34]. However, for the Nb-Ti-V-Zr system the respective ternaries were not assessed, instead being extrapolations from the assessed binaries. The equilibrium microstructures were predicted between 200 – 2500 K.

2.1.3 Density functional theory

A plane wave density functional theory package, VASP [35,36], was chosen as it will reproduce the intermetallic/metallic nature of the bonding to satisfactory accuracy. It has been successfully used in the past to model HEAs and other metallic systems [14,37–39]. A 0.02 \AA^{-1} k -point density with a Methfessel-Paxton smearing method (0.125 eV) was used. The projector augmented wave (PAW) method with the exchange correlation functional described by the generalised gradient approximation (GGA) as developed by Perdew-Burke-Ernzerhof (PBE) [40] was used. Spin-polarization effects were also considered; no magnetisation was observed in any systems examined. The semi-core p electrons were treated as valence electrons for Nb, Ti and V and semi-core s electrons for Zr. A cut-off energy of 350 eV and the electronic and geometric convergence criterion were 10^{-7} eV and 10^{-6} eV, respectively, for constant pressure calculations.

Supercells of body-centred-cubic (BCC) structure consisting of 54 atoms were constructed and the atomic positions were assigned using the special quasi-random structure (SQS) method as implemented in the ATAT toolkit [41]. The average properties of five SQS supercells were taken to represent the bulk HEA for compositions $\text{Nb}_{0.31}\text{Ti}_{0.26}\text{V}_{0.28}\text{Zr}_{0.15}$, $\text{Nb}_{0.26}\text{Ti}_{0.24}\text{V}_{0.24}\text{Zr}_{0.26}$, $\text{Nb}_{0.20}\text{Ti}_{0.20}\text{V}_{0.19}\text{Zr}_{0.41}$ (aligned to the experimental analysis of the homogenised samples). This method has been used with much success in previous works [29,42–45]. CrystalMaker™ was used to simulate XRD patterns of the relaxed DFT models.

The properties of each composition were assessed using the stress-strain method [46] implemented within VASP. The energy cutoff was increased to 600 eV to converge the stress tensor on fully relaxed constant volume structures. Six finite distortions were imposed to the lowest energy supercell of each composition, and each atom was displaced once by 0.015 Å in both the $\pm x$, $\pm y$ and $\pm z$ directions (totalling 648 calculations on each composition) to obtain the contributions to the elastic constants by the ionic relaxations. The polycrystalline elastic moduli: shear modulus (G), bulk modulus (B), Young's modulus (E) and Poisson's ratio (ν) were then calculated using the Hill's approach with Voigt's and Reuss's approximations [47].

2.2 Experimental

2.2.1 Arc melting and thermal treatments

The set of three alloys were prepared by weighing the pure elements according to their target stoichiometries to a total of ~25 g. These pure metal mixtures were then placed in an Edmund Buhler Arc Melter, which consisted of a water-cooled copper crucible with a W electrode. The whole system was contained within a hermetically sealed steel cylinder with a 10^{-3} mTorr vacuum and Ar partial pressure of 800 mTorr. A maximum current of 250 A was applied to the samples, which were melted for 5 minutes. After the samples solidified, the resulting button of material was flipped and the procedure repeated. The button was flipped a total of 4 times. The as-cast buttons were sectioned into 5-10×5×5 mm pieces for heat treatment and analysis. For heat-treatment, samples were wrapped in Mo foil of 0.1 mm thickness and encapsulated in a silica glass evacuated and backfilled with Ar gas. The as-cast samples were homogenised at $1200\pm 10^\circ\text{C}$ (1473 ± 10 K) for 100 hrs and water quenched. Their densities were measured by the Archimedes method, comparing the submerged and unsubmerged weights in water at room temperature. These samples were subsequently sectioned and aged at $700\pm 10^\circ\text{C}$ (973 ± 10 K) for 100 hrs.

2.2.2 Scanning electron microscopy and energy dispersive x-ray spectroscopy

The arc melted, homogenised and aged samples were analysed using scanning electron microscopy (SEM) with a JEOL JSM-6010LA operated at 20 kV accelerating voltage, equipped with an energy dispersive X-ray spectroscopy (EDS) detector, while a ZEISS AURIGA operated at 10 kV was used to obtain higher magnification backscattered electron (BSE) images (see Table 1).

Table 1. Energy dispersive x-ray spectroscopy measurements of the alloys by large area scans, average \pm standard deviation.

Alloy designation		Nb (at. %)	Ti (at. %)	V (at. %)	Zr (at. %)
Zr_{0.5}HEA	nominal	28.6	28.6	28.6	14.2
	measured	32.4 \pm 2.6	26.6 \pm 0.2	27.4 \pm 0.8	13.7 \pm 1.8
ZrHEA	nominal	25.0	25.0	25.0	25.0
	measured	25.7 \pm 0.2	23.8 \pm 0.1	24.0 \pm 0.1	26.6 \pm 0.1
Zr₂HEA	nominal	20.0	20.0	20.0	40.0
	measured	20.0 \pm 0.3	19.4 \pm 0.1	20.4 \pm 0.5	40.3 \pm 0.2

2.2.3 X-ray diffraction

A BRUKER D2 PHASER with Cu- α X-ray source was used to collect reflections between angles 8-105° with step size of 0.03° 2 θ on a rotating stage. Pattern fitting was applied within the X'Pert HighScore Plus framework to obtain peak positions. The lattice parameter of each phase was estimated using the Nelson-Riley method [48].

2.2.4 Transmission electron microscopy

Transmission electron microscopy (TEM) samples were prepared from thin discs cut from a 3mm cylinder, subsequently ground to 0.20-0.25 mm in thickness. Electropolishing was performed using a Struers TenuPol with a solution of 10% perchloric acid in methanol at -30°C and 20 V. Scanning TEM (STEM) and high-angle annular dark-field imaging (HAADF) were then performed on JEOL JEM-2100F operated at 200 kV, equipped with an Oxford Instruments energy dispersive X-ray spectroscopy (EDS) detector. Elemental maps and point scan measurements were collected on the aged samples tilted to 15° using the Oxford Instruments AZtec software package, collected qualitative ‘TruMaps’ were 512 \times 512 pixels with a dwell time of 5 ms/pixel, as well as quantified point scans using the Cliff-Lorimer method k-factors within Aztec.

2.2.5 Indentation measurements

Indentation hardness was obtained on a Zwick Roell Indentec 6030 LKV Vickers hardness tester using a diamond Vickers tip. All indents were made at 1 kg load for 10 s. Nanoindentation testing was performed on a Nanotest Platform 2 nanoindenter (MicroMaterials, UK). Nanoindentation was performed on all homogenised HEA samples and on reference samples of Zircaloy-4 (Zr-4) and 316 L stainless steel (316 SS). Indentations were conducted on the polished faces of the samples, which were mounted in bakelite. Artefacts arising from the comparatively low-stiffness of the bakelite were eliminated by ensuring the specimen width was >1,000 times the indent depth, following calculations by Yan et al. [49]. The Berkovich tip’s area function was calibrated using fused silica, accounting for the frame compliance (0.328 nm/mN). Each indent consisted of a 30 s loading phase to a maximum load of 10 mN, a 30 s hold at maximum load, and a 30 s unload. Thermal drift was corrected for during the unload phase, using a 60 s hold at 10% of maximum load. Each sample measured with 10

indents, which were separated by at least 5 times their width. The Young's modulus was calculated according to the Oliver-Pharr method [50].

3. Results and discussion

3.1 Alloy search and predict (ASAP)

As a first-order high throughput screening method, ‘alloy search and predict’ (ASAP) [25] was used to assess 1,028,790 four-element equimolar combinations from 72 elements of the periodic table. These combinations were ranked in order of smallest to largest microscopic thermal neutron absorption cross section, σ_A , calculated as the weighted sum of the pure elements [51]. Fig. 1 includes the 100,000 combinations with the lowest linear combination of microscopic thermal neutron absorption cross-section. Combinations that satisfy the two criteria $\Phi > 1$ and $\delta \leq 6.6$ are predicted to form a single-phase disordered solid-solution phase at the melting temperature. The majority of these combinations exist outside these bounds due to the alloys that have the lowest σ_A being a mixture of metals and non-metals, e.g., C, Be, Bi, Mg, Pb, Si, P, Zr, Al and H (ranked from lowest to highest).

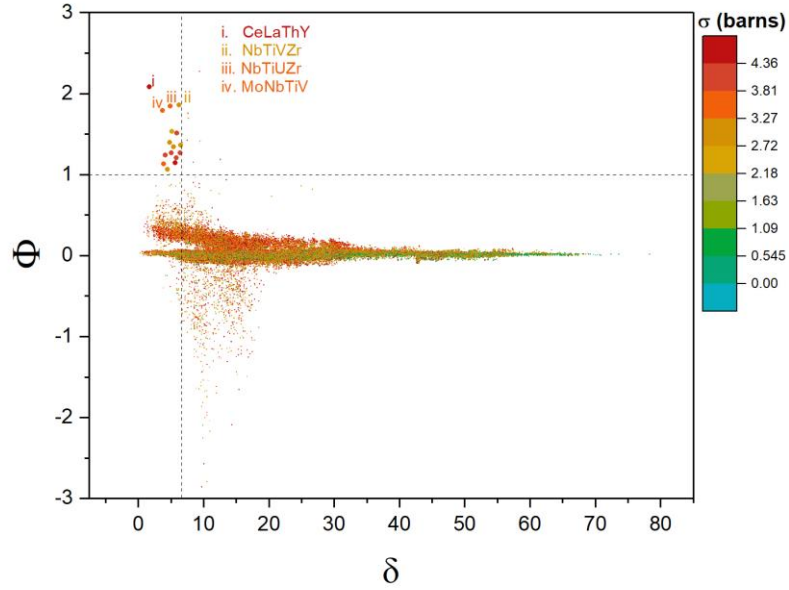


Fig. 1. The single-phase solid-solution formability predicted from a thermodynamic assessment (y-axis) and variation in atomic radii (x-axis), where a single-phase solid-solution is predicted for $\Phi \geq 1$ and $\delta \leq 6.6$, of the 100,000 equimolar four-element combinations that have the lowest microscopic thermal neutron absorption cross-section. The top four most stable compositions are labelled i – iv and their constituent elements are stated. Corresponding dataset accessible at ref. [52].

Neglecting the combinations that consist of atomically unstable elements, NbTiVZr is the primary candidate alloy that possesses both a single-phase and high neutron transparency. Of the four elements within this system, Zr has the lowest σ (0.185 barns) followed by Nb (1.15 barns), V (5.08

barns) and Ti (6.09 barns). To assess the effect of variation of Zr (representing the most neutron transparent of the four elements) on the system, three stoichiometries were investigated with Zr contents of 0.5, 1 and 2 atomic ratio to the other elements. The information output by ASAP for these three stoichiometries can be seen in Table 2. It is predicted that the formation of a single-phase HEA is possible when the Zr content is varied from 0.5-2.0 atomic ratio. However, the δ parameter increases with increasing Zr content and is close to the threshold (6.60) of single-phase formability as suggested by Yang *et al.* [11].

Table 2. ASAP outputs: Φ (stability), δ (atomic radii deviation), σ_A (thermal neutron absorption cross-section), VEC (valence electron concentration), H_{max} (binary with most unfavourable enthalpy of mixing), H_{mix}^p (enthalpy of mixing of likely precipitate), H_{mix}^{ss} (enthalpy of mixing of solid-solution phase), T_p (precipitate temperature) and T_m (melting temperature), for the three alloys investigated within this study.

System	Φ	δ	σ_A (barns)	VEC	$H_{max(A-B)}$	H_{mix}^p (kJ/mol)	H_{mix}^{ss} (kJ/mol)	T_p (K)	T_m (K)
Zr _{0.5} HEA	2.22	5.7	3.55	4.57	Nb-Zr	5.19	2.41	1138	2261
Zr ₁ HEA	1.86	6.27	3.13	4.50	Nb-Zr	5.89	4.02	1370	2245
Zr ₂ HEA	2.01	6.55	2.54	4.40	Nb-Zr	4.72	5.61	1358	2221

The lower temperature behaviour predicted by ASAP is made by a comparison between formation energy of the complete solid-solution and the binary intermetallic phases of the system. Therefore, for systems without any obvious intermetallic phases, the precipitation temperature (T_p) is considered unreliable. However, the enthalpy of mixing of the hypothetical precipitate, H_{mix}^p provides insight into the temperature behaviour of the system [14]. For the case of Zr_{0.5}HEA, Zr₁HEA and Zr₂HEA, the Nb-Zr binary has the largest magnitude of H_{mix}^p between the possible binaries of the system, and is a positive value, suggesting that the unfavourable mixing between Nb and Zr and is reflected by the miscibility gap in its binary phase diagram [53].

Many single-phase HEAs are stabilised at elevated temperatures and may precipitate or phase separate when aged at lower temperatures (823 – 1473 K) [40–47]. The calculated enthalpies of mixing for the solid-solution phases, H_{mix}^{ss} , of Zr_{0.5}HEA, Zr₁HEA and Zr₂HEA, are all positive and therefore require entropy to stabilise. The temperatures at which allotropic transformations from BCC to hexagonal close packed (HCP) occur, as observed in Zr and Ti [54], or phase separation, observed in Nb and Zr alloys [55], are important to consider for these systems and are examined using Computer Coupling of Phase Diagrams and Thermochemistry (CALPHAD) in the next section.

3.2 Calculated equilibrium phases

Predictions from CALPHAD (Thermocalc™) are now presented and discussed. Although the ternaries that belong to this system are not assessed, the solid-solution enthalpies are extrapolated

from the binary systems and segregation phenomena are considered. As such, caution must be exercised when comparing these to experimental findings, as discussed later. Fig. 2 shows the predicted phases and their volume fractions, between temperatures 300 – 2500 K, for $\text{Zr}_{0.5}\text{HEA}$, ZrHEA and Zr_2HEA , under equilibrium conditions. In agreement with ASAP, a single-phase BCC region was predicted below the melting temperature for the three alloys, and which was stable across a wide temperature range. The boundary at which this single-phase separated into a dual phase microstructure was predicted to occur at 878 K, 1000 K and 1060 K, in order of increasing Zr content. At lower temperatures (<700 K) alpha phase was predicted, promoted by the allotropic transformations for Ti and Zr. Further, the V_2Zr Laves phase is predicted to precipitate. However, at temperatures <800 K, due to sluggish kinetics, long ageing times may be required to reach equilibrium [56]. Conversely, when subjected to neutron irradiation the kinetics may be accelerated [57,58]. It is therefore necessary to investigate the intermediate temperature behaviour experimentally and assess the accuracy of the theoretical predictions.

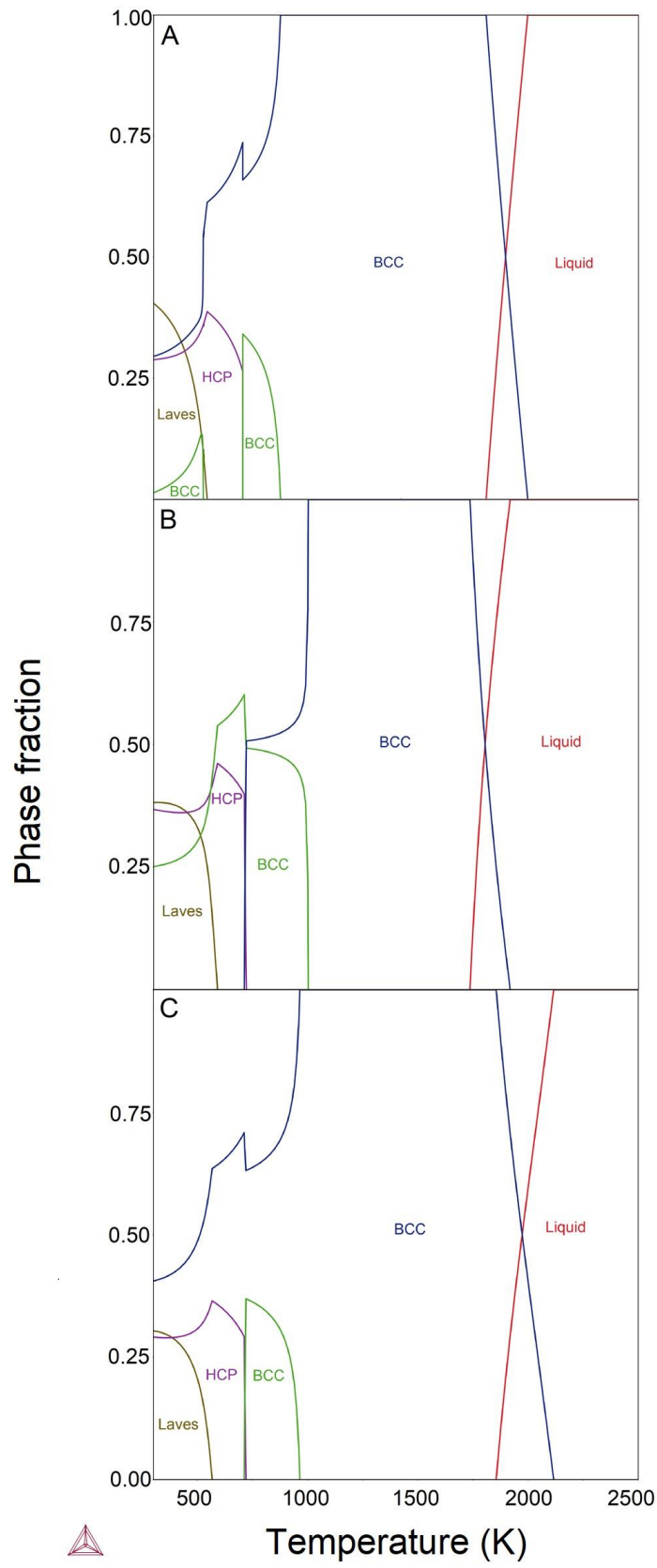


Fig. 2. Predicted equilibrium phase diagram of (A) Zr_{0.5}HEA, (B) Zr₁HEA and (C) Zr₂HEA for temperatures between 300 – 2500 K. The structure of each respective phase is written within its enclosing line.

3.3 *As-cast and homogenised microstructures*

The three NbTiVZr_x ($x = 0.5, 1, 2$) HEAs were produced by arc melting, and heat treatments applied to explore whether they exist as single-phase BCC experimentally. The as-cast and homogenised samples exhibited XRD patterns with only BCC reflections, see Fig. 3. Density functional theory simulations were performed on BCC models of the three compositions. A comparison of the lattice parameters between as-cast, homogenised and simulation is made in

Fig. 4. The simulated XRD patterns of the relaxed DFT models correspond well to the experimental results. An exact match is not expected due to the approximate nature of the exchange-correlation functional [59]. Further, due to the periodic nature of the DFT calculations, superlattice ordering peaks are present. However, no such peaks were observable in the experimental patterns, suggesting that a disordered BCC solid-solution was achieved. The low intensity of the (202) and (310) reflections in both as-cast and homogenised samples was due to the long homogenisation time where excessive grain growth occurred resulting in a large grain size of >1 mm. A slight shift in peak positions to higher 2θ values was observed between the as-cast and homogenised structures likely due to the attainment of more homogenous elemental redistribution to a more complete mixing and relief from the residual macro stresses imposed during the arc melting and quench process.

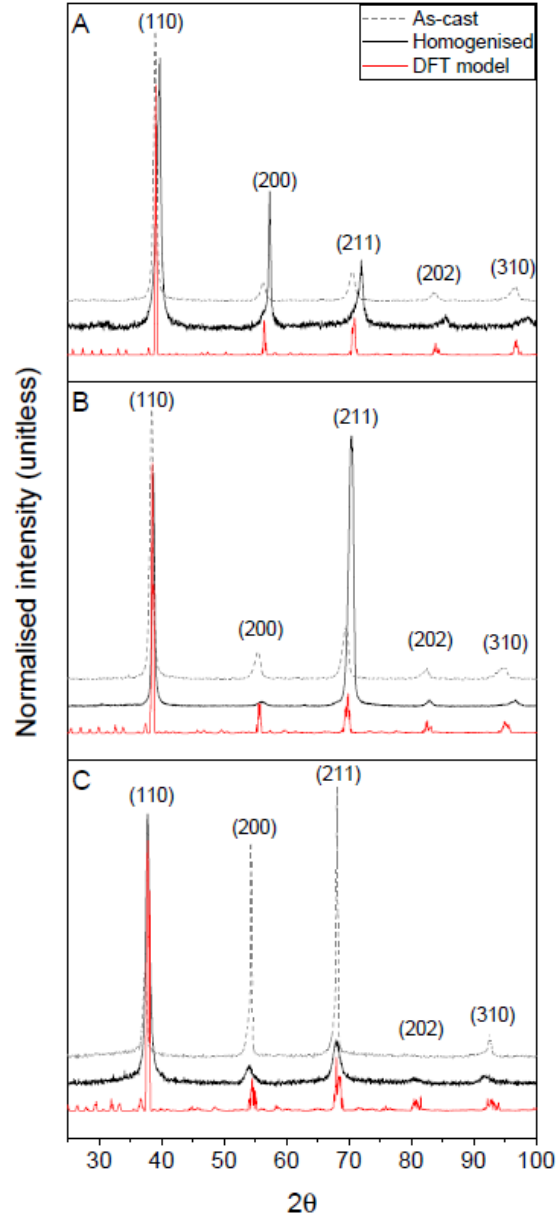


Fig. 3. X-ray diffraction pattern of (A) Zr_{0.5}HEA, (B) ZrHEA and (C) Zr₂HEA in the as-cast (dashed grey), homogenized (solid black) and simulated (solid red) conditions.

Fig. 4 provides a comparison of the lattice parameter obtained by various methods. All samples exhibit the same trend of increasing lattice parameter with Zr content (where pure Zr has the largest

atomic radii). The lattice parameter of the equimolar composition is replicated using the same level of theory as Tian *et al.* [60]. There is a $\sim 6 \times 10^{-3}$ nm difference between the experimentally measured lattice parameter of the homogenised equimolar composition compared to the measurement of Senkov *et al.* [26]. This difference is likely due to the differing homogenisation methods that led to different microstructure, i.e., hot isostatic pressing followed by cooling at 10 K/min, while in this study samples were water quenched. Furthermore, Senkov *et al.* showed extensive secondary phase formation, while this is not the case this study, as will be shown later in this paper.

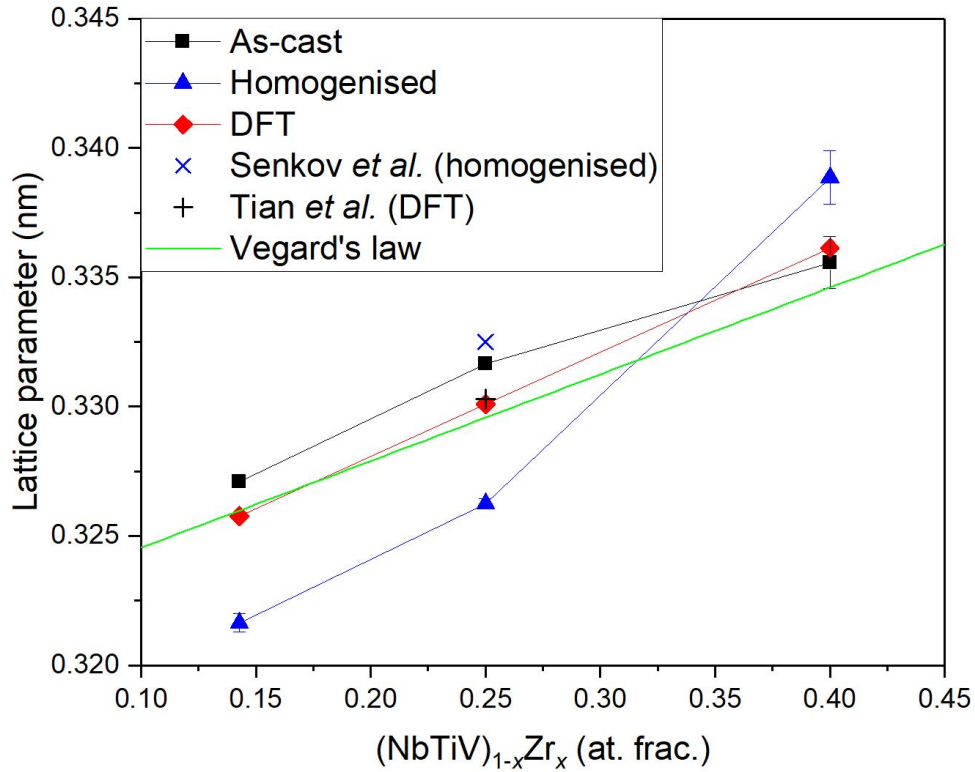


Fig. 4. Lattice parameter with varying Zr experimentally measured in the as-cast (black square) and homogenized (blue triangle), compared to calculated values from Vegard's law (green line) and DFT (red diamond).

Scanning electron microscopy in the as-cast condition using backscatter imaging revealed the alloys had a dendritic morphology (Fig. 5(A-C)) with dendrite coring and microsegregation. Composition measurements using EDS line scans showed the segregation of the highest melting temperature element, Nb (2720 K [61]), to the dendrites, and the lowest, Zr (2127 K [61]), to the interdendritic regions, with the Ti and V concentrations comparatively homogenous, see Fig. 5.

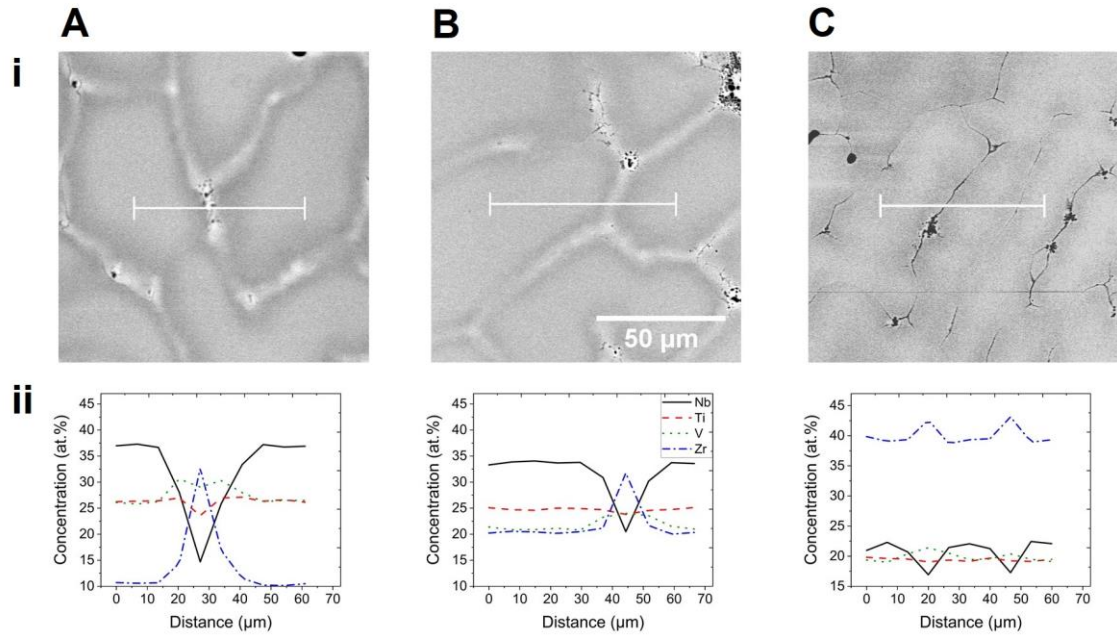


Fig. 5. EDS line scan measurements across the interdendritic regions for as-cast (A) $\text{Zr}_{0.5}\text{HEA}$, (B) ZrHEA and (C) Zr_2HEA showing the (i) BSE images and (ii) corresponding composition measurements of Nb (solid line), Ti (dashed line), V (dotted line), and Zr (dashed and dotted line).

Homogenisation of the samples at 1200°C (1473 K), resulted in the formation of a single-phase solid-solution, see Fig. 6. The XRD patterns (Fig. 3) again indicated solely BCC reflections. However, in contrast to Fig. 5ii, line scan measurements revealed no composition variations. The single-phase state of the alloy at 1200°C is further evidenced by the extensive grain growth and lack of contrast under BSE and SE imaging (Fig. 6(A-C)), with no second-phase observed even at higher magnifications. This is in contrast to previous reports of the equiatomic NbTiVZr HEA [26,62]. The absence of these features in the current study is attributed to the rapid cooling rate employed ($\sim 100\text{ K s}^{-1}$) compared to the previous studies ($\sim 10\text{ K min}^{-1}$). To test this hypothesis, a sample of ZrHEA was furnace cooled after homogenisation and, indeed, micro-segregation was observed, see Ref. [63].

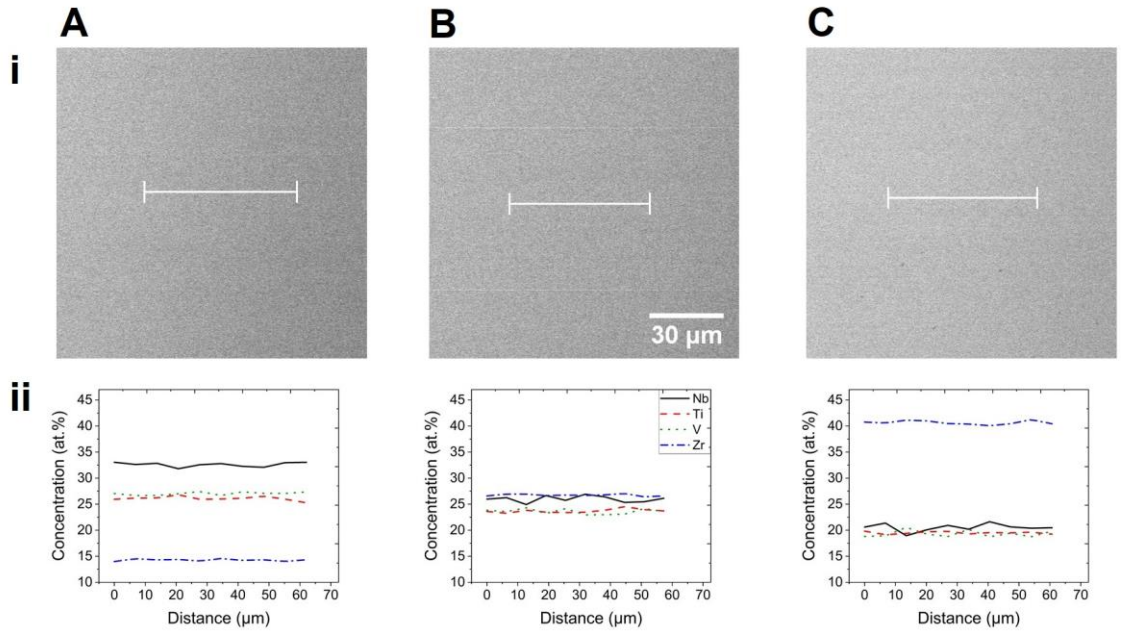


Fig. 6. EDS line scan measurements of the HEAs in the 1200°C homogenised condition (A) Zr_{0.5}HEA, (B) ZrHEA and (C) Zr₂HEA showing the (i) BSE images and (ii) corresponding composition measurements of Nb (solid line), Ti (dashed line), V (dotted line), and Zr (dashed and dotted line).

In agreement with ASAP and CALPHAD, the three HEAs can indeed exist as single-phase BCC solid-solutions, devoid of microsegregation induced by casting. It is reasonable to conclude that the success of the homogenisation process is sensitive to the cooling-rate thereafter: diffusion kinetics – contentiously believed to be sluggish in HEAs [64,65] – are actually sufficiently fast for elements to segregate into secondary phases over short time periods [16,66,67].

3.4 Thermal ageing at 700°C

Aging of the alloys was performed at 700°C (973 K) for 100 h to determine whether the BCC single-phase solid-solution is stable at intermediate temperature. Although this temperature is considerably higher than nominal light water reactor temperatures (350-400°C) these materials could conceivably be exposed to a temperature of this order in transient or gen. IV reactor environments.

Here, it was found that the alloys experienced significant solute redistribution and phase transformations. Fig. 7 shows XRD patterns of the three aged alloys. In Zr_{0.5}HEA reflections corresponding to two phases (HCP and BCC) were identified; while for Zr₁HEA three phases (HCP, BCC and V₂Zr Laves); and for Zr₂HEA four phases (HCP, 2 BCCs and V₂Zr laves) were identified. The peaks attributed to the C15 Fd-3m V₂Zr Laves phase [68,69] were fitted with a lattice parameter $a \sim 7.396 \text{ \AA}$, for which not all reflections were present due to a combination of their structure factor and the sample's texture. These multi-phase structures were in agreement with SEM BSE imaging, where multi-phase nano-scale microstructures were observed, see Fig. 8.

HAADF-STEM imaging revealed the multi-phase microstructures indicated by SEM-BSE in greater detail, see Fig. 9. A trend of coarser phases with increased Zr content was noted: $\text{Zr}_{0.5}\text{HEA}$ 190 ± 50 nm; Zr_1HEA 270 ± 90 nm; Zr_2HEA 330 ± 120 nm, attributed to the trend of lower alloy melting temperature (Table 2) and so commensurately faster diffusion kinetics at 973 K. Composite images were produced by stacking individual elemental maps of Nb, Ti, V and Zr of the three aged samples. For all samples, the number of stable phases observed in HAADF and composite images agrees with the number identified by XRD. In $\text{Zr}_{0.5}\text{HEA}$ and Zr_1HEA , the blue phase corresponds to enrichment with HCP-stabilising Ti and Zr and hence was attributed to the HCP phase, while the yellow phase enriched with BCC-stabilising V, was attributed to the BCC phase. In Zr_1HEA and Zr_2HEA , the composition of the pink phase (Table 3) led to its attribution as V_2Zr laves phase, with off-stoichiometric solubility for Ti and Nb [68]. In Zr_2HEA , the yellow phase and blue phase were attributed to two BCC phases due to their enrichment in BCC-stabilising V, while the purple phase was attributed to the HCP phase owing to enrichment in HCP-stabilising Ti and Zr.

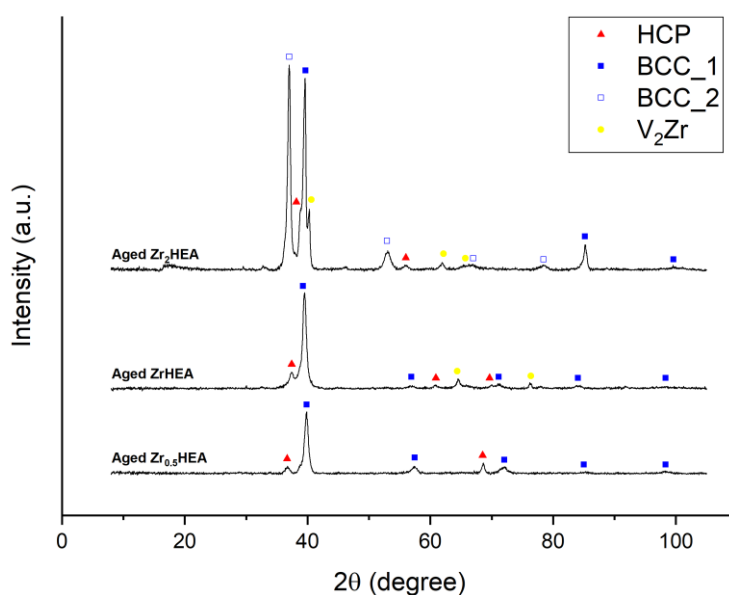


Fig. 7. X-ray diffraction patterns of thermally aged $\text{Zr}_{0.5}\text{HEA}$, ZrHEA and Zr_2HEA with peaks corresponding to HCP (red triangle), BCC_1 (blue square), BCC_2 (blue hollow square) and V_2Zr laves phase (yellow circle)

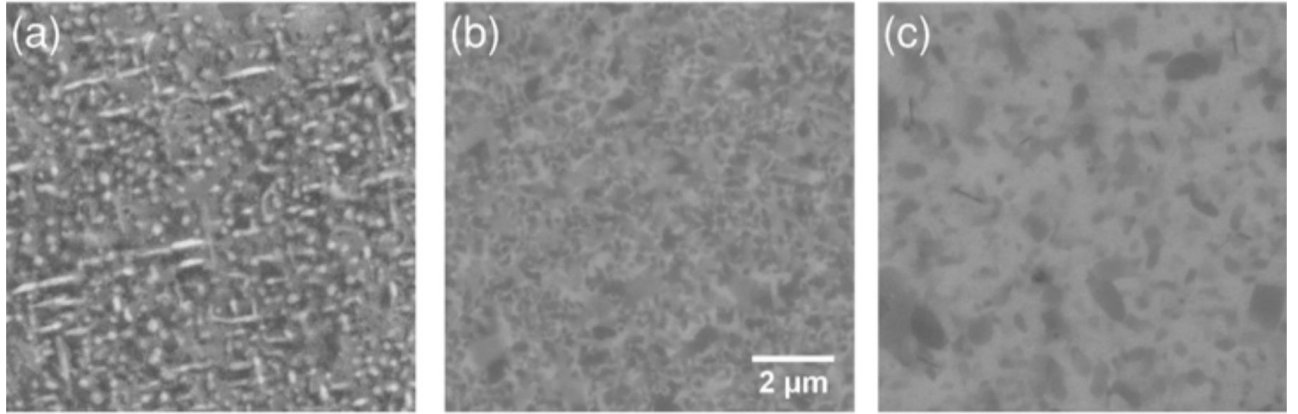


Fig. 8. Scanning electron microscopy backscattered electron micrographs of (a) $Zr_{0.5}HEA$, (b) Zr_1HEA and (c) Zr_2HEA after thermal ageing at 700°C for 100 h.

Table 3. Stable phases observed in aged $Zr_{0.5}HEA$, Zr_1HEA and Zr_2HEA

Alloy	Phase colour (composite image)	Nb (at. %)	Ti (at. %)	V (at. %)	Zr (at. %)	Number of EDS points	Attributed crystal structure
$Zr_{0.5}HEA$	Blue	12.8±0.9	40.2±0.3	15.7±4	31.3±4.6	3	HCP
	Yellow	17.9±0.5	37.6±0.3	37.6±1.4	7.0±1.9	4	BCC
$ZrHEA$	Blue	13.2±0.4	43.4±0.5	13.7±1.2	29.8±2	2	HCP
	Yellow	17.5±0.9	43.1±0.1	27.4±2.7	12.0±3.5	2	BCC
	Pink	11.0±0.2	9.7±0.1	59.9±0.5	19.4±0.3	4	V_2Zr
Zr_2HEA	Blue	11.6±0.2	18.2±2.2	46.6±2.6	23.6±0.6	2	BCC
	Yellow	15.6	26.9	41.6	15.9	1	BCC
	Pink	11.0±0.1	9.2±0.1	59.6±0.1	20.1±0.2	3	V_2Zr
	Purple	13.3±0.1	42.5±0.5	11.5±0.2	32.7±0.6	6	HCP

In the CALPHAD prediction, neither HCP nor V_2Zr Laves phases were present at this temperature but were predicted at lower temperatures (see Table 4). Experimentally, at 973 K HCP structures were observed in all three compositions and Laves phase in Zr_1HEA and Zr_2HEA . In their pure forms, Zr and Ti undergo allotropic transformations from BCC \rightarrow HCP below 1135 K and 1153 K, respectively, and in the V-Zr binary system V_2Zr is thermodynamically stable below 1573 K. Whilst useful to give an indication of possible phases, the TCHEA2 database does not accurately capture the change of behaviour of these phenomena with alloying, largely owing to the lack of assessed ternaries.

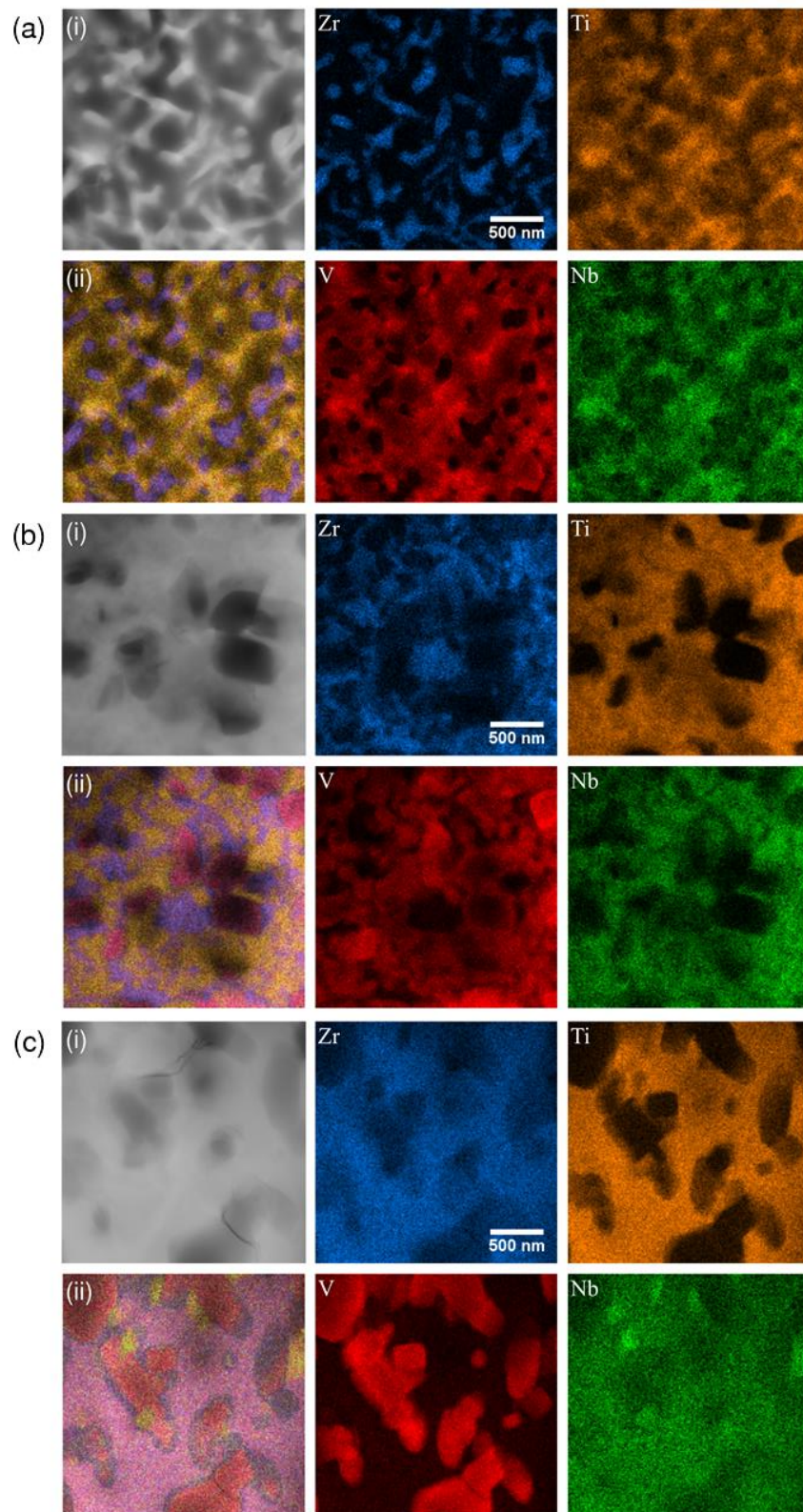


Fig. 9. TEM analysis of aged (a) $Zr_{0.5}HEA$, (b) Zr_1HEA and (c) Zr_2HEA with their respective (i) HAADF-STEM image (upper-left) and (ii) composite image (lower-left) obtained from stacking qualitative elemental maps of Zr (upper-middle), Ti (upper-right), V (lower-middle) and Nb (lower-right).

Table 4. Stable phase(s) at 973 K in CALPHAD prediction and identified XRD patterns

Alloy	CALPHAD prediction	XRD patterns
Zr_{0.5}HEA	BCC	BCC + HCP
ZrHEA	2 BCC	BCC + HCP + V ₂ Zr laves
Zr₂HEA	2 BCC	2 BCC + HCP + V ₂ Zr laves

3.5 Hardness and Young's modulus

To gain a preliminary assessment of the mechanical properties of the HEA samples, micro and nano-indentation was performed and compared to Zircaloy-4 and type 316 stainless steel (referred to as Zr-4 and 316 SS, respectively). Fig. 10 compares the micro-hardness values measured for the as-cast, homogenised, aged HEA samples, 316 and Zr-4. The hardness of the HEA samples are more than double that of the two commercial alloys. The overall range in hardness values of the HEAs is from 3.05-3.65 GPa (311.2-372.6 HV), which is in agreement with past literature measurement of 3.29 GPa for the NbTiVZr stoichiometry [27]. A trend of increasing hardness with Zr content is seen for the heat-treated conditions and there is only a small change in average hardness between the as-cast and homogenised conditions (≤ 0.09 GPa), and aged conditions (≤ 0.26 GPa). The lack of significant strengthening following ageing, despite the development of multi-phase precipitates (Figure 9), suggests that any Orowan particle strengthening is negated by a loss of solid solution strengthening in the bcc matrix, as minimal grain growth occurred at 700°C. Fig. 10 also shows hardness data of the alloys measured by nano-indentation that are 4-11% larger than the values obtained by micro-hardness measurements, this slight increase is likely due to indentation size effect [70].

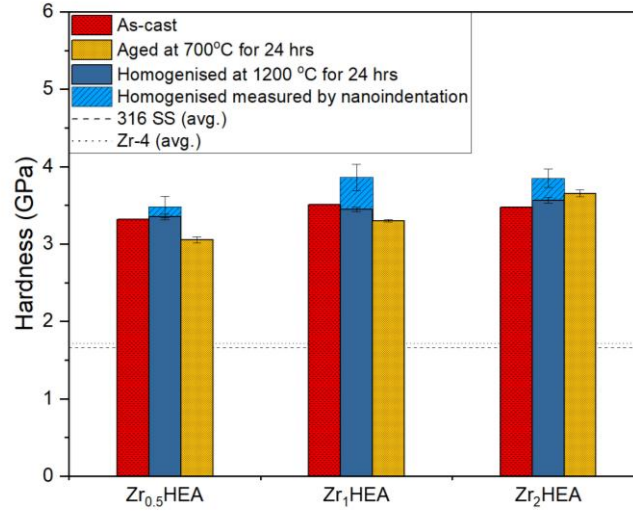


Fig. 10. Microhardness values measured for Zr_{0.5}HEA, ZrHEA and Zr₂HEA (x-axis) for as-cast (red), homogenised (blue) and aged (yellow) condition with associated standard deviation in measurement. Combined range in hardness for measurements of 316 and Zr-4 are included as a grey horizontal region.

Table 5 presents elastic moduli (determined by DFT) of the HEAs in their homogenised condition, and those of BCC Fe and BCC Zr. These are compared to the Young's moduli measured by nanoindentation on the homogenised HEA samples, 316 SS and Zr-4. Interestingly, the Young's modulus for Zr₂HEA is the lowest of the three HEAs using both modelling and experimental techniques, although the absolute magnitudes differ by 10-18 % between methods. When compared to past DFT studies of the equimolar HEA by Qui *et al.* and Liao *et al.*, the Young's and shear moduli calculated in the current study are slightly larger and bulk modulus slightly lower. This is likely caused by the different supercell sizes between the studies [71]. In the work by Tian *et al.* [72] the Young's and shear moduli are significantly lower ~50% than calculated by the former two studies and current study. We attribute this to the underestimation of C_{44} within their study, see Table A.1 (appendix).

When comparing to the commercial alloys the Young's moduli of the HEAs are approximately 10-20% lower than that of Zr-4 and are approximately half that of 316 SS and CoCrFeMnNi (203 GPa [73]) a popular face-centered cubic HEA. It should be noted that the nanoindentation measurements overestimate the moduli of the two conventional alloys compared to their materials datasheet (by 10 and 14% for 316 SS and Zr-4, respectively). Despite this overestimation and accounting for the standard deviation in measurement, the equimolar sample produced in the current study has a slightly larger Young's modulus than the sample studied by Senkov *et al.* (80 GPa) [27], which is likely due to the slight deviations from nominal composition and aforementioned differences in homogenisation techniques.

Table 5. Density functional theory calculated elastic moduli: Bulk (B), shear (G) and Young's (E), and Poisson's ratio (ν) for the homogenised HEA compositions. Young's modulus obtained by nanoindentation (E_{nano}) included for comparison.

Composition			B (GPa)	G (GPa)	E (GPa)	E_{nano} (GPa)*	ν	B/G
Zr_{0.5}HEA			135.3	30.7	85.8	101±2	0.39	4.4
	Current study		117.6	41.9	112.4	102±3	0.34	2.8
ZrHEA	a		129.5	20.1	57.3	-	0.43	6.4
	Literature	b	132.0	34.4	95.1	-	0.38	3.8
		c	133.1	30.7	85.6	-	0.38	4.5
Zr₂HEA			113.4	29.4	81.1	92±2	0.38	3.9
Zr_{BCC}			89.0	35.9	94.9	113±8*	0.32	2.5
Fe			181.0	79.5	208.1	212±13*	0.31	2.3

^a relaxed SQS cells using VASP by Tian *et al.* [72]

^b relaxed SQS cells using VASP by Qui *et al.* [74]

^c relaxed structure using virtual crystal approximation in CASTEP by Liao *et al.* [75]

* E_{nano} measurement was performed on an alloy and DFT calculation was performed on pure element.

Overall, the mechanical property measurements reported here show a clear strength advantage of Zr-based HEAs as compared to commercial Zr-4. Indeed, pioneering work by Senkov *et al.* has shown that a multiphase equimolar sample of NbTiVZr can achieve compressive strengths of ≤ 1000 MPa and 50% compression without fracture at 873 K [27]. However, it should be noted that a non-negligible ductile-to-brittle transition temperature may exist for these HEAs due to their BCC structure [76]. In what follows, this mechanical strength information is collated with neutron absorption cross-section data to develop a figure-of-merit that accounts for both properties, which will allow a comparison of alloys' performance.

3.6 Technological relevance

A theoretical prediction of the *macroscopic* thermal neutron absorption cross-section, Σ_A , of an alloy can be made by taking the weighted average of the *microscopic* thermal neutron absorption cross-section, σ_A , measured from neutron experiments on the pure metals [51], of the elements that constitute the alloy and then multiply by the molar material density, [77]:

$$\Sigma_A = \frac{\rho N_a}{M} \sum_i (n_i \sigma_{Ai}) \quad (2)$$

where ρ is the physical density, N_a is Avogadro's number, M the mass of one mole of alloy atoms, n_i the atomic fraction of element i , and σ_{Ai} the neutron absorption cross-section for the case of thermal neutrons.

The pristine densities of Zr_{0.5}HEA, Zr₁HEA and Zr₂HEA are calculated to be 6.70, 6.60 and 6.53 g/cm³, respectively, by DFT. The respective experimentally measured densities of the

homogenised samples were 6.32, 6.35, 6.39 g/cm³. The density of the equimolar sample measured by Senkov *et al.* [26] (6.52 g/cm³) was much closer to the theoretical result, likely due to the use of the hot isostatic press method of homogenisation.

A prediction of Σ_A is made using the densities measured experimentally within the current study, see Table 6. It is clear that Zr-4 has a lower Σ_A than the HEAs and 316 SS by two orders of magnitude. When considering the hardness and moduli of each material in combination with Σ_A , i.e. H/Σ_A and E/Σ_A , these figures of merit (FOM) rank the HEAs as a more superior candidate than 316 SS for the former and worse in the latter.

Table 6. Comparison of microscopic thermal neutron absorption cross section (σ_A), density (ρ) and macroscopic thermal neutron absorption cross section (Σ_A).

Alloy	σ (barns) [51]	ρ (g/cm ³)	Σ_A (m ⁻¹)	FOM $\left(\frac{H}{\Sigma \times 100}\right)$	FOM $\left(\frac{E}{\Sigma \times 100}\right)$
Zr_{0.5}HEA	3.55	6.32	2.00×10 ⁻³	18	582
ZrHEA	3.13	6.35	1.69×10 ⁻³	22	638
Zr₂HEA	2.54	6.39	1.31×10 ⁻³	29	788
Zr-4	0.20	6.56 [78]	8.78×10 ⁻⁵	2279	125358
316 SS	3.04	~7.90 [61]	2.59×10 ⁻³	8	811

Steels are used as cladding materials in fast reactors [79] and are candidate cladding materials for advanced sodium/lead cooled fast reactors and supercritical water reactors [80]. Considering Σ_A alone, it is unlikely that a HEA of the Nb-Ti-V-Zr system will be favoured as a cladding material in a thermal fission reactor over Zr alloys. However, it is plausible that they could be used in fast reactor environments for load bearing or coating applications. This is especially true if they offer some advantage over steels or other accident tolerant fuel candidates, e.g. higher strengths, increased radiation tolerance, high temperature stability/mechanical properties, or can be alloyed to achieve better corrosion and oxidation resistance [81].

In terms of temperature stability, the use of these HEAs in the homogenised condition is predicted to be unfeasible for medium temperature applications (600-1000 K). This is because the single-phase region is small and the kinetics are sufficient for equilibrium to be achieved in short timeframes and the HEAs will adopt a multiphase microstructure below ~1000 K. Conversely, these alloys may be suitable for lower temperature applications (room temperature-600 K) with a multiphase microstructure as hardness measurements do not predict a significant change in material behaviour relative to the homogenised condition.

4. Conclusions

- (1) A new high throughput screening tool, *Alloy Search and Predict* (ASAP), has been used to predict that the Nb-Ti-V-Zr system would have the highest single phase stability of the 100,000 lowest thermal neutron cross-section of the four-element systems, constituted of atomically stable elements. The NbTiVZr_x series, where $x = 0.5$ (Zr_{0.5}HEA), 1 (Zr₁HEA), and 2 (Zr₂HEA), were then investigated using a range of experimental and theoretical techniques. Thermocalc (using the TCHEA2 database) predicted the single-phase region for Zr_{0.5}HEA, Zr₁HEA and Zr₂HEA, to be stable from the solidus to ~1000 K; below which, spinodal decomposition into Nb/Zr rich/poor solid-solution phases, allotropic transformations of Ti and Zr from BCC to HCP, and precipitation of the V₂Zr C15 Laves phase will occur.
- (2) Experimental evaluation of the NbTiVZr_x ($x = 0.5, 1, 2$) type HEAs confirmed that this is a single-phase HEA system. Homogenisation at 1200°C for 100 h resulted in a single-phase BCC microstructure without the compositional microsegregation present in as-cast or slow cooled samples. The lattice parameters of the as-cast, homogenised and DFT simulated models were all in relative agreement and followed the trend predicted by Vegard's law. It was found that fast cooling was needed to prevent elemental redistribution, indicating that the single-phase field does not extend to room temperature.
- (3) Aging of the alloys to simulate potential reactor temperatures, identified that at 700°C all three ZrHEA decompose into multiple phases. X-ray diffraction and STEM-EDX indicated that BCC miscibility gaps, allotropic transformation from BCC to HCP and precipitation of V₂Zr C15 Laves phase, which can each be related back to the binary systems, Zr-Nb, Zr-Ti and Zr-V, respectively. There was no clear increase in hardness, despite an anticipated strengthening effect from the formation of multiple nano-scale phases on aging.
- (4) Industrial application of this alloy system remains a possibility owing to the significant hardness and small melting point benefit over commercially available zirconium alloys. These offer the prospects of increased high temperature strength and reduced creep rates. Whilst the neutron cross-sections of the alloys are markedly higher than Zr, the combination of properties required for future advanced nuclear reactors operating at increased temperatures may be advantageous. Further work will be needed to evaluate the capability of these new multi-phase alloys and the optimum property trade-off.

Acknowledgements:

AJK was funded by a EUROfusion Researcher Grant Fellowship. STYC was funded by a CCFE and Imperial College Faculty of Engineering UROP Award. SAHB was funded by an Imperial College Research Fellowship. This research was undertaken with the assistance of resources provided by the EPSRC Tier 2 allocation on CSD3 (Skylake and KNL) HPCs, Australian National

Computational Infrastructure provided by UNSW (Raijin) and Imperial College Tier 2 computing (Cx1 and Cx2). The authors would also wish to acknowledge the technical assistance provided by Tim Lucey, Kim Lu, Tim Palmer, Joel Davis and Rob Aughterson.

References

- [1] J.W. Yeh, Y.L. Chen, S.J. Lin, S.K. Chen, High-entropy alloys - A new era of exploitation, *Adv. Struct. Mater.* III. 560 (2007) 1–9.
- [2] B. Cantor, I. Chang, P. Knight, A. Vincent, Microstructural development in equiatomic multicomponent alloys, *Mater. Sci. Eng. A.* (2004) 213–218.
- [3] B. Gludovatz, A. Hohenwarter, D. Catoor, E.H. Chang, E.P. George, R.O. Ritchie, A fracture-resistant high-entropy alloy for cryogenic applications, *Science* (80-.). 345 (2014) 1153–1158.
- [4] X.Z. Lim, Metal mixology, *Nature*. 533 (2016) 306–307.
- [5] Z. Li, K.G. Pradeep, Y. Deng, D. Raabe, C.C. Tasan, Metastable high-entropy dual-phase alloys overcome the strength–ductility trade-off, *Nature*. 534 (2016) 227.
- [6] Y. Yao, Z. Huang, P. Xie, S.D. Lacey, R.J. Jacob, H. Xie, F. Chen, A. Nie, T. Pu, M. Rehwoldt, Carbothermal shock synthesis of high-entropy-alloy nanoparticles, *Science* (80-.). 359 (2018) 1489–1494.
- [7] Y.J. Zhou, Y. Zhang, Y.L. Wang, G.L. Chen, Microstructure and compressive properties of multicomponent $\text{Al}_x(\text{TiVCrMnFeCoNiCu})_{100-x}$ high-entropy alloys, *Mater. Sci. Eng. A.* 454–455 (2007) 260–265.
- [8] B.S. Li, Y.P. Wang, M.X. Ren, C. Yang, H.Z. Fu, Effects of Mn, Ti and V on the microstructure and properties of AlCrFeCoNiCu high entropy alloy, *Mater. Sci. Eng. A.* 498 (2008) 482–486.
- [9] Y.-L. Chen, Y.-H. Hu, C.-A. Hsieh, J.-W. Yeh, S.-K. Chen, Competition between elements during mechanical alloying in an octonary multi-principal-element alloy system, *J. Alloys Compd.* 481 (2009) 768–775.
- [10] Z. Wang, S. Guo, C.T. Liu, Phase Selection in High-Entropy Alloys: From Nonequilibrium to Equilibrium, *JOM*. 66 (2014) 1966–1972.
- [11] X. Yang, Y. Zhang, Prediction of high-entropy stabilized solid-solution in multi-component alloys, *Mater. Chem. Phys.* (2012) 233–238.
- [12] M.C. Tropicovsky, J.R. Morris, P.R.C. Kent, A.R. Lupini, G.M. Stocks, Criteria for Predicting the Formation of Single-Phase High-Entropy Alloys, *Phys. Rev. X.* 5 (2015) 11041.
- [13] O.N. Senkov, J.D. Miller, D.B. Miracle, C. Woodward, Accelerated exploration of multi-principal element alloys with solid solution phases, *Nat Commun.* 6 (2015) 6529.
- [14] D.J.M. King, S.C. Middleburgh, A.G. McGregor, M.B. Cortie, Predicting the formation and stability of single phase high-entropy alloys, *Acta Mater.* 104 (2016) 172–179.
- [15] D. Ma, B. Grabowski, F. Körmann, J. Neugebauer, D. Raabe, Ab initio thermodynamics of the CoCrFeMnNi high entropy alloy: Importance of entropy contributions beyond the configurational one, *Acta Mater.* 100 (2015) 90–97.
- [16] E.J. Pickering, N.G. Jones, High-entropy alloys: a critical assessment of their founding principles and future prospects, *Int. Mater. Rev.* (2016) 1–20.
- [17] T. Egami, W. Guo, P.D. Rack, T. Nagase, Irradiation Resistance of Multicomponent Alloys, *Metall. Mater. Trans. A.* 45 (2014) 180–183.

- [18] S. Xia, Z. Wang, T. Yang, Y. Zhang, Irradiation Behavior in High Entropy Alloys, *J. Iron Steel Res. Int.* 22 (2015) 879–884.
- [19] T. Yang, S. Xia, W. Guo, R. Hu, J.D. Poplawsky, G. Sha, Y. Fang, Z. Yan, C. Wang, C. Li, Effects of temperature on the irradiation responses of Al 0.1 CoCrFeNi high entropy alloy, *Scr. Mater.* 144 (2018) 31–35.
- [20] C. Smith, *Nuclear Reactor Materials*, Addison-Wesley, Detroit, 1967.
- [21] V. Urbanic, T. Heidrick, High-temperature oxidation of Zircaloy-2 and Zircaloy-4 in steam, *J. Nucl. Mater.* (1978) 251–261.
- [22] F.J.E.J.S. Leistikow, Zircaloy Fuel Cladding Behavior in a LOCA -A Review, in: *Zircon. Nucl. Ind. Seventh Int. Symp.*, ASTM International, 1985: pp. 24–27.
- [23] T. Allen, J. Busby, M. Meyer, D. Petti, Material challenges for nuclear systems, *Mater. Today.* 13 (2010) 15–23.
- [24] S.J. Zinkle, G.S. Was, Materials challenges in nuclear energy, *Acta Mater.* 61 (2013) 735–758.
- [25] D.J.M. King, A.G. McGregor, Alloy Search And Predict (ASAP), [Http://Www.Alloyasap.Com](http://www.alloyasap.com). (2015).
- [26] O.N. Senkov, S. V Senkova, C. Woodward, D.B. Miracle, Low-density, refractory multi-principal element alloys of the Cr-Nb-Ti-V-Zr system: Microstructure and phase analysis, *Acta Mater.* 61 (2013) 1545–1557.
- [27] O.N. Senkov, S. V Senkova, D.B. Miracle, C. Woodward, Mechanical properties of low-density, refractory multi-principal element alloys of the Cr-Nb-Ti-V-Zr system, *Mater. Sci. Eng. a-Structural Mater. Prop. Microstruct. Process.* 565 (2013) 51–62.
- [28] D.J.M. King, Investigation of high-entropy alloys for use in advanced nuclear applications, University of Technology, 2016.
- [29] D.M. King, S.C. Middleburgh, L. Edwards, G.R. Lumpkin, M. Cortie, Predicting the Crystal Structure and Phase Transitions in High-Entropy Alloys, *JOM.* 67 (2015) 2375–2380.
- [30] F.R. de Boer, *Cohesion in metals: transition metal alloys*, North-Holland ; Sole distributors for the U.S.A. and Canada, Elsevier Scientific Pub. Co., Amsterdam ; New York : New York, N.Y., U.S.A., 1988.
- [31] H. Bakker, *Enthalpies in Alloys: Miedema's Semi-empirical Model*, Trans Tech Publications, 1998.
- [32] Y. Zhang, Y.J. Zhou, J.P. Lin, G.L. Chen, P.K. Liaw, Solid-solution phase formation rules for multi-component alloys, *Adv. Eng. Mater.* 10 (2008) 534–538.
- [33] A.K. Singh, N. Kumar, A. Dwivedi, A. Subramaniam, A geometrical parameter for the formation of disordered solid solutions in multi-component alloys, *Intermetallics.* 53 (2014) 112–119.
- [34] D.B. Miracle, J.D. Miller, O.N. Senkov, C. Woodward, M.D. Uchic, J. Tiley, Exploration and Development of High Entropy Alloys for Structural Applications, *Entropy.* 16 (2014) 494–525.
- [35] G. Kresse, J. Hafner, Ab initio molecular-dynamics for liquid-metals, *Phys. Rev. B.* (1993) 558–561.
- [36] G. Kresse, J. Hafner, Ab-initio molecular-dynamics simulation of the liquid-metal amorphous semiconductor transition in germanium, *Phys. Rev. B.* (1994) 14251–14269.
- [37] Y. Zhang, T.T. Zuo, Y.Q. Cheng, P.K. Liaw, High-entropy Alloys with High Saturation Magnetization, Electrical Resistivity, and Malleability, *Sci. Rep.* 3 (2013) 7.
- [38] F.Y. Tian, L.K. Varga, N.X. Chen, J. Shen, L. Vitos, Ab initio design of elastically isotropic TiZrNbMoVx high-entropy alloys, *J. Alloys Compd.* 599 (2014) 19–25.
- [39] S.C. Middleburgh, D.M. King, G.R. Lumpkin, M. Cortie, L. Edwards, Segregation and migration of

- species in the CrCoFeNi high entropy alloy, *J. Alloys Compd.* 599 (2014) 179–182.
- [40] J.P. Perdew, K. Burke, M. Ernzerhof, Generalized Gradient Approximation Made Simple, *Phys. Rev. Lett.* 77 (1996) 3865–3868.
 - [41] A. Van de Walle, P. Tiwary, M. De Jong, D.L. Olmsted, M. Asta, A. Dick, D. Shin, Y. Wang, L.-Q. Chen, Z.-K. Liu, Efficient stochastic generation of special quasirandom structures, *Calphad.* 42 (2013) 13–18.
 - [42] C. Niu, A.J. Zaddach, A.A. Oni, X. Sang, J.W. Hurt, J.M. LeBeau, C.C. Koch, D.L. Irving, Spin-driven ordering of Cr in the equiatomic high entropy alloy NiFeCrCo, *Appl. Phys. Lett.* 106 (2015) 161906.
 - [43] D.J.M. King, P.A. Burr, E.G. Obbard, S.C. Middleburgh, DFT study of the hexagonal high-entropy alloy fission product system, *J. Nucl. Mater.* 488 (2017) 70–74.
 - [44] D.J.M. King, P.A. Burr, S.C. Middleburgh, T.M. Whiting, M.G. Burke, M.R. Wenman, The formation and structure of Fe-Mn-Ni-Si solute clusters and G-phase precipitates in steels, *J. Nucl. Mater.* 505 (2018) 1–6.
 - [45] Z. Leong, J.S. Wróbel, S.L. Dudarev, R. Goodall, I. Todd, D. Nguyen-Manh, The Effect of Electronic Structure on the Phases Present in High Entropy Alloys, *Sci. Rep.* 7 (2017) 39803.
 - [46] Y. Le Page, P. Saxe, Symmetry-general least-squares extraction of elastic data for strained materials from ab initio calculations of stress, *Phys. Rev. B.* 65 (2002) 104104.
 - [47] G. Grimvall, *Thermophysical properties of materials*, Elsevier, 1999.
 - [48] J.B. Nelson, JB Nelson and DP Riley, *Proc. Phys. Soc. London* 57, 477 (1945)., in: *Proc. Phys. Soc. London*, 1945: p. 477.
 - [49] W. Yan, C.L. Pun, G.P. Simon, Conditions of applying Oliver–Pharr method to the nanoindentation of particles in composites, *Compos. Sci. Technol.* 72 (2012) 1147–1152.
 - [50] W.C. Oliver, G.M. Pharr, An improved technique for determining hardness and elastic modulus using load and displacement sensing indentation experiments, *J. Mater. Res.* 7 (1992) 1564–1583.
 - [51] V. Sears, Neutron scattering lengths and cross sections, *Neutron News.* (1992) 29–37.
 - [52] D.J.M. King, Alloy Search and Predict outputs for 100,000 equimolar four-element combinations with the lowest microscopic thermal neutron absorption cross-section, *Mendeley Data*, V1. (2018).
 - [53] H. Okamoto, Nb-Zr (niobium-zirconium), *J. Phase Equilibria.* 13 (1992) 577.
 - [54] D.A. Young, *Phase Diagrams of the Elements*, University of California, Virginia, USA, 1975.
 - [55] J. Sopousek, M. Svobodová, Thermodynamic Prediction of Zr-Nb-OH Phase Diagram Sections, in: *Solid State Phenom.*, Trans Tech Publ, 2011: pp. 487–492.
 - [56] C. Ng, S. Guo, J. Luan, S. Shi, C. Liu, Entropy-driven phase stability and slow diffusion kinetics in an Al_{0.5}CoCrCuFeNi high entropy alloy, *Intermetallics.* (2012) 165–172.
 - [57] P.R. Okamoto, L.E. Rehn, Radiation-induced segregation in binary and ternary alloys, *J. Nucl. Mater.* 83 (1979) 2–23.
 - [58] J. Lee, C.R. Lear, X. Zhang, P. Bellon, R.S. Averback, Irradiation-Induced Nanoprecipitation in Ni-W Alloys, *Metall. Mater. Trans. A.* 46 (2015) 1046–1061.
 - [59] L. He, F. Liu, G. Hautier, M.J.T. Oliveira, M.A.L. Marques, F.D. Vila, J.J. Rehr, G.-M. Rignanese, A. Zhou, Accuracy of generalized gradient approximation functionals for density-functional perturbation theory calculations, *Phys. Rev. B.* 89 (2014) 64305.
 - [60] H.J. Ge, F.Y. Tian, Y. Wang, Elastic and thermal properties of refractory high-entropy alloys from first-principles calculations, *Comput. Mater. Sci.* 128 (2017) 185–190.

- [61] W.M. Haynes, CRC handbook of chemistry and physics, CRC press, 2014.
- [62] O.N. Senkov, S. Rao, K.J. Chaput, C. Woodward, Compositional effect on microstructure and properties of NbTiZr-based complex concentrated alloys, *Acta Mater.* 151 (2018) 201–215.
- [63] C. Parkin, D.J.M. King, A.J. Knowles, A. Couet, Data on the annealing of NbTiVZr at 1200°C with slow cooling rate, *Data in Brief.* (in Review) 2019.
- [64] T.T. Shun, C.H. Hung, C.F. Lee, Formation of ordered/disordered nanoparticles in FCC high entropy alloys, *J. Alloys Compd.* 493 (2010) 105–109.
- [65] K. Tsai, M. Tsai, J. Yeh, Sluggish diffusion in Co-Cr-Fe-Mn-Ni high-entropy alloys, *Acta Mater.* (2013) 4887–4897.
- [66] F.J. Wang, Y. Zhang, G.L. Chen, H.A. Davies, Cooling rate and size effect on the microstructure and mechanical properties of AlCoCrFeNi high entropy alloy, *J. Eng. Mater. Technol.* 131 (2009) 34501.
- [67] S. Singh, N. Wanderka, B. Murty, U. Glatzel, J. Banhart, Decomposition in multi-component AlCoCrCuFe high entropy alloy, *Acta Mater.* (2011) 182–190.
- [68] M. Enomoto, The Ti-V-Zr System, *J. Phase Equilibria.* (1992) 206–210.
- [69] D.J.M. King, S.C. Middleburgh, A.C.Y. Liu, H.A. Tahini, G.R. Lumpkin, M.B. Cortie, Formation and structure of V–Zr amorphous alloy thin films, *Acta Mater.* 83 (2015) 269–275.
- [70] W.D. Nix, H. Gao, Indentation size effects in crystalline materials: a law for strain gradient plasticity, *J. Mech. Phys. Solids.* 46 (1998) 411–425.
- [71] F. Tasnádi, M. Odén, I.A. Abrikosov, Ab initio elastic tensor of cubic Ti_{0.5}Al_{0.5}N alloys: dependence of elastic constants on size and shape of the supercell model and their convergence, *Phys. Rev. B.* 85 (2012) 144112.
- [72] L.Y. Tian, G.S. Wang, J.S. Harris, D.L. Irving, J.J. Zhao, L. Vitos, Alloying effect on the elastic properties of refractory high-entropy alloys, *Mater. Des.* 114 (2017) 243–252.
- [73] G. Laplanche, P. Gadaud, O. Horst, F. Otto, G. Eggeler, E.P. George, Temperature dependencies of the elastic moduli and thermal expansion coefficient of an equiatomic, single-phase CoCrFeMnNi high-entropy alloy, *J. Alloys Compd.* 623 (2015) 348–353.
- [74] S. Qiu, N. Miao, J. Zhou, Z. Guo, Z. Sun, Strengthening mechanism of aluminum on elastic properties of NbVTiZr high-entropy alloys, *Intermetallics.* 92 (2018) 7–14.
- [75] M. Liao, Y. Liu, L. Min, Z. Lai, T. Han, D. Yang, J. Zhu, Alloying effect on phase stability, elastic and thermodynamic properties of Nb-Ti-V-Zr high entropy alloy, *Intermetallics.* 101 (2018) 152–164.
- [76] D.B. Miracle, O.N. Senkov, A critical review of high entropy alloys and related concepts, *Acta Mater.* 122 (2017) 448–511.
- [77] P. Rinard, Neutron interactions with matter, in: R. D, E. N, S. H, K. S (Eds.), *Passiv. Nondestruct. Assay Nucl. Mater.*, NUREG/CR-5550, US Nuclear Regulatory Commission, Washington, DC, 1991.
- [78] Allegheny Technologies Incorporated, *Reactor Grade Zirconium*, Pittsburgh, 2015.
- [79] R.L. Klueh, Ferritic/martensitic steels for advanced nuclear reactors, *Trans. Indian Inst. Met.* 62 (2009) 81–87.
- [80] P. Yvon, F. Carré, Structural materials challenges for advanced reactor systems, *J. Nucl. Mater.* (2009) 217–222.
- [81] T.M. Butler, J.P. Alfano, R.L. Martens, M. Weaver, High-Temperature Oxidation Behavior of Al-Co-Cr-Ni-(Fe or Si) Multicomponent High-Entropy Alloys, *Jom.* 67 (2015) 246–259.

Appendix

Table A.1. The elastic constants (C_{11} , C_{12} and C_{44}) as calculated by DFT in the current study for $\text{Zr}_{0.5}\text{HEA}$, Zr_1HEA , Zr_2HEA , Fe_{BCC} and Zr_{BCC} . Past results from DFT calculations for Zr_1HEA are compared.

Alloy	$\text{Zr}_{0.5}\text{HEA}$ (GPa)	Zr_1HEA (GPa)				Zr_2HEA (GPa)	Fe_{BCC} (GPa)	Zr_{BCC} (GPa)
		Current study	a	b	c			
C_{11}	181.4	177.5	159.8	174.4	149.7	147.2	270.2	153.2
C_{12}	112.0	87.6	114.3	109.4	124.8	96.6	136.6	57.0
C_{44}	28.4	40.0	18.5	31.9	55.4	32.5	89.8	29.5

^a relaxed SQS cells using VASP by Tian *et al.* [72]

^b relaxed SQS cells using VASP by Qui *et al.* [74]

^c relaxed structure using virtual crystal approximation in CASTEP by Liao *et al.* [75]